Journal of *Marine Science and Engineering*

MDPI

Article

Analysis of Microscopic Characteristics of Marine Clay Under Salinity Influence: ESEM, Zeta Potential and DLS Tests

Shuai Yuan [1], Yi Shan [1,2,*], Zhirong Lu [1], He'an Xie [3], Yadong Li [1,2,*] and Jie Cui [1,2]

[1] School of Civil Engineering and Transportation, Guangzhou University, Guangzhou 510006, China; 2112316069@e.gzhu.edu.cn (S.Y.); luzhirong14@163.com (Z.L.); jcui@gzhu.edu.cn (J.C.)
[2] A Guangdong Engineering Research Center for Underground Infrastructural Protection in Coastal Clay Area, Guangzhou 510006, China
[3] HUASEN Engineering Technology Group Co., Ltd., Zhaotong 657002, China; m13422111845@163.com
* Correspondence: yshan@gzhu.edu.cn (Y.S.); liyadong@gzhu.edu.cn (Y.L.)

Abstract

Marine clay serves as the natural foundation for various types of offshore and marine engineering structures and therefore plays a critical role in marine engineering practice. Consequently, a thorough understanding of the microstructural characteristics of marine clay is of great importance. In this study, two types of artificial marine clays with high and low clay contents were selected. Environmental scanning electron microscopy (ESEM), zeta potential measurements, and dynamic light scattering (DLS) tests were conducted to investigate the microstructure, surface electrical potential, and aggregation behavior of marine clay. The results revealed that the high-clay-content sample exhibited more compact particle connections, while the low-clay-content sample displayed a relatively loose structure. The addition of salt altered the particle distribution within the soil, increasing the aggregation of fine clay particles, which in turn compressed the diffuse double layer between particles. This caused changes in the surface electrokinetic potential of clay mineral particles and enhanced the stability of the soil samples. DLS tests on the high-clay-content sample showed that the aggregation state of clay particles was highly sensitive to salinity, with particle size initially increasing and then decreasing as salinity increased.

Keywords: aggregation; marine clay; microstructure; salinity; zeta potential

1. Introduction

In recent years, a wide range of offshore and marine engineering projects have developed rapidly [1,2]. Among the different types of clay, marine clay is a special type closely related to marine environments. Marine clay typically refers to clay deposited in a marine environment, containing seawater components. Its main constituents are clay minerals such as montmorillonite, kaolinite, and illite, and it often contains significant amounts of salt. In coastal engineering, marine clay exhibits typical characteristics such as low shear strength, high compressibility, and high sensitivity [3]. It is affected by factors such as salinity, tidal forces, and earthquakes, which, in turn, influence its macroscopic mechanical properties [4]. These factors can jeopardize the safety and long-term performance of marine infrastructure. Therefore, understanding its microstructural characteristics is of significant engineering importance.

Microstructural morphology is a key entry point for revealing the aggregation state of clay particles and the characteristics of pore structures [5]. Conventional scanning electron microscopy (SEM) tests usually require sample pretreatment such as drying, which can

Check for updates

Academic Editor: Kai Yao

Received: 5 February 2026
Revised: 21 March 2026
Accepted: 24 March 2026
Published: 26 March 2026

Copyright: © 2026 by the authors. Licensee MDPI, Basel, Switzerland. This article is an open access article distributed under the terms and conditions of the Creative Commons Attribution (CC BY) license.

readily alter the aggregation state of clay particles and cause the collapse of micropores, thereby failing to accurately reflect the original microstructural features under natural or engineering conditions. In contrast, ESEM does not require complex pretreatment and enables direct observation of clay particle morphology, size, degree of aggregation, and pore distribution under near-natural temperature and humidity conditions. This effectively avoids damage to the microstructure caused by sample preparation and provides a reliable technique for the accurate characterization of clay microstructures [6]. Based on the results of microstructural tests, the pore structure and microstructural characteristics of soils can be systematically analyzed.

Zeta potential, as a key parameter characterizing the surface electrochemical properties of clay particles [7], reflects the surface charge state, electrical double-layer structure, and the strength of interparticle interactions. It directly influences the dispersibility, stability, sedimentation behavior of clay particles, as well as their interfacial interactions with other substances. The outcomes of these microstructural characterizations can be evaluated in a coordinated manner and further applied to macroscopic-scale analyses. In recent years, an increasing number of studies have incorporated microstructural tests (such as ESEM and Zeta potential measurements) into investigations of soil mechanical behavior. For example, Javaheri et al. [8] integrated SEM observations into rheological testing to elucidate the relationship between salt-induced changes in soil rheological properties and microstructural stability, highlighting the importance of combining rheological and microstructural tests in soil hazard research. McFarlane et al. [9] employed SEM to investigate the effects of different ionic solutions on the microstructural state of montmorillonite and subsequently analyzed the mechanisms responsible for variations in rheological behavior. Markgraf et al. [10] demonstrated that particle charge density (PCD) theory is closely related to Zeta potential, and quantitatively analyzed microstructural changes in saline fluids using rheological and particle charge techniques, thereby confirming that Zeta potential measurements can be used for the quantitative assessment of particle aggregation. Baumgarten et al. [11] utilized electrokinetic measurements to analyze soil aggregation strength and mechanisms, as well as thixotropy and microstructural stability. The experimental results of Ni et al. [12] showed that variations in soil viscoelastic properties were consistent with changes in Zeta potential, confirming the effectiveness of Zeta potential and electrical double-layer theory in elucidating soil viscoelastic behavior. Luckham and Rossi [13], focusing on Na^+-montmorillonite suspensions, demonstrated that microscopic factors such as particle aggregation state and interparticle interaction forces exert a pronounced influence on yield stress. Salinity and mineral composition are key factors affecting the mechanical properties of marine clay [14–16]. By integrating ESEM observations with Zeta potential measurements, this study systematically characterizes the microstructural morphology and surface electrochemical properties of clays with different mineral compositions under varying salinity conditions. The intrinsic relationship between clay particle aggregation states and Zeta potential is explored, and the coupled effects of clay microstructure and surface charge characteristics are elucidated. These findings provide accurate experimental data support and theoretical references for enhancing the engineering performance of clay materials, as well as for advancing fundamental research in related fields.

Dynamic light scattering (DLS) is based on the principles of light scattering and Brownian motion [17]. It can effectively characterize the aggregation behavior of clay particles under different solution concentrations. DLS enables rapid and non-destructive capture of changes in the aggregation state of colloidal systems in an aqueous environment [18], and is therefore particularly suitable for investigating the evolution of aggregate size in fine-grained, marine-clay–dominated materials under varying salinity (ionic strength) conditions. The addition of salt alters the thickness of the electrical double layer, thereby

affecting interparticle interactions [19,20]. Accordingly, aggregation behavior can be used to assess the underlying mechanisms of particle–particle interactions. However, existing studies on the salinity effects of marine clays have largely focused on relatively low salt concentrations, and investigations on the aggregation of clay minerals under high-salinity conditions remain scarce [16]. This area is still underexplored, and the aggregation mechanisms of marine clays induced by salinity variations are not yet well understood. Therefore, it is necessary to conduct DLS tests on marine clays. Moreover, DLS can be cross-correlated with ESEM and zeta (ζ) potential measurements: ESEM provides microscale evidence of pore-structure evolution, zeta potential characterizes particle surface charge and interfacial electrochemical conditions, and DLS quantitatively captures the resulting structural manifestation (i.e., aggregation/aggregate-size characteristics). Together, these techniques constitute an integrated experimental framework, providing critical microscale evidence for interpreting salinity-controlled clay structural stability and the associated evolution of engineering properties.

This study selected two groups of artificial marine clays with significantly different clay mass fractions for comparative investigation. ESEM was employed to obtain microstructural information of the different soil samples, and image-processing techniques were applied to extract porosity parameters for quantitative characterization of the soil microstructure. Next, Zeta potential measurements were conducted under different salinity conditions to determine the Zeta potential of soil particles, characterizing the electrical double-layer structure and its response to changes in ionic strength, thereby providing an electrochemical basis for explaining the variations in interparticle interaction forces. Finally, DLS tests were performed to investigate the effective hydrodynamic diameter of colloidal particles under different salinity conditions and its temporal evolution, enabling quantitative assessment of the influence of salinity on the aggregation state of marine clay particles.

2. Materials and Methods

2.1. Materials

Based on a systematic review of existing relevant research literature and the field investigation results from the Guangdong-Hong Kong-Macao Greater Bay Area's targeted site surveys of marine areas, this region's marine sedimentary clays exhibit typical heterogeneous characteristics in their mineral composition [21]. The mineral composition of marine sedimentary clay in this region exhibits a typical multi-component mixed characteristic, with the main constituting minerals including quartz and feldspar, two typical non-clay minerals, as well as various layered silicate clay minerals such as montmorillonite, kaolinite, illite, and chlorite [22]. These minerals play a critical role in the mechanical properties, physical characteristics, and interactions with water in the soil. The proportion and occurrence of different mineral components directly determine the microstructure and macroscopic mechanical response of the marine sedimentary clay, which is also the core reason for the significant regional differences in its rheological properties. Following the relevant criteria of mineral classification, this study has established a four-component artificial synthesis system, which includes two types of non-clay minerals, quartz (Q) and feldspar (F), as well as two types of clay minerals, montmorillonite (M) and kaolinite (K) [23]. The parameters of the four minerals are shown in Table 1.

The mineral raw materials used in this test were sourced from natural minerals produced by Hunyuan Junhong New Materials Co., Ltd. (Guangzhou, China) To accurately replicate the mineral composition characteristics of typical marine clays, a mineral phase ratio control method was employed. By specifically adjusting the blending ratios of different mineral phases, a simulated system was constructed that closely matches the mineral

composition of the target marine clay. Two soil samples with significant compositional differences were prepared: a high-clay-content sample (ratio code: $Q_8F_2M_{15}K_{15}$) and a low-clay-content sample (ratio code: $Q_{24}F_6M_5K_5$). These samples serve as test groups for subsequent multi-dimensional comparative analysis. The numerical values corresponding to the codes represent the mass proportions of each mineral in every 40g of soil. For example, the mineral mass ratio for the high-clay-content sample ($Q_8F_2M_{15}K_{15}$) is Q:F:M:K = 8:2:15:15 (g).

Table 1. Mineral parameters.

Mineral	Specific Surface Area Ss (m^2/g)	Cation Exchange Capacity (CEC) ($cmol^+/kg$)	Mineral Phase Analyses (RIR Method for Calculating Phase Fraction)
Quartz	2.198	0.9	97.21% quartz 2.79% mica
Feldspar	1.193	1.5	85.33% albite 14.67% orthoclase
Montmorillonite	16.332	103.3	90.03% Na-montmorillonite 8.22% quartz 1.75% calcite
Kaolinite	14.925	4.8	93.32% kaolinite 6.68% Dickite

Deionized water was pre-prepared using the YMK40201A distiller (Fuyao Group, Guangzhou, China). After cooling to room temperature, it was sealed and stored in a beaker for use in subsequent experiments. To prepare marine clay samples under different pore water salinity conditions, a series of saline solutions with varying concentration gradients were required. Since sodium chloride (NaCl) is the primary soluble salt in natural seawater, all saline solutions in this study were prepared using analytical-grade granular sodium chloride (purity > 99.5%) from China National Pharmaceutical Group Corporation (Beijing, China) as the solute. The concentration of the saline solutions is expressed as a mass percentage. For example, a 10% saline solution means that each 100 g of the solution contains 10 g of solid sodium chloride. Five test concentrations were set for this study: 0%, 1%, 2.5%, 5%, and 10%.

2.2. Microscopic Tests

2.2.1. Environmental Scanning Electron Microscopy (ESEM) Tests

Based on the principle of non-disturbed microstructural observation [12], this study used an ESEM (QUANTA200, FEI Company, Hillsboro, OR, USA) to observe the microstructure of two soil samples with different salinities. The soil samples used in the test were the aforementioned two types of mixed soil samples. The soil samples were fully saturated and free from mechanical loading disturbance, which can effectively avoid irreversible plastic failure and structural degradation caused by mechanical actions and ensure the integrity and fidelity of the original information of the microstructural parameters.

The test procedure is as follows:

(a) A pair of tweezers was taken, and petroleum jelly was evenly applied to its tips. Then, a 7 mm × 7 mm cutting area was marked in the center of the soil samples. A blade was used to carefully trim the edges of the marked area, ultimately preparing a standard soil sample with dimensions of 5 mm × 5 mm.

(b) The prepared soil sample was securely fixed onto the observation platform using double-sided carbon conductive adhesive. The surface of the sample was gently brushed with an air blower to remove any loose particles and impurities. Once

the cleaning was completed, the entire observation platform with the sample was transferred into the test instrument.

(c) The instrument's operational parameters were adjusted to the preset range. After the vacuum level inside the instrument chamber reached the desired value, the microstructure of the sample surface was observed. Image capture and data recording were then completed.

2.2.2. Zeta Potential Tests

Zeta potential is the electrokinetic potential at the shear plane of the double-layer structure of colloidal particles. Its magnitude and sign directly determine the charged characteristics and the charge intensity of the colloidal particles [24]. In this study, the Zeta potential of soil particles was measured using the Zetasizer Nano ZS90 (Malvern Instruments, Malvern, UK). This instrument utilizes the principle of electrophoresis to accurately measure the potential parameters.

In the specific testing process, the soil particle dispersion was placed in the electrolyte testing system of the instrument, followed by the application of a stable, uniform electric field to the system. At this point, the charged soil particles in the suspension would move in a direction towards the electrode with the opposite charge, driven by the electric field force. Meanwhile, the interactions between the particles, such as Van der Waals forces and electrostatic forces, as well as the frictional forces between the particles and the electrolyte medium, would generate viscous resistance, hindering the electrophoretic movement of the particles. When the electrostatic driving force and the viscous resistance reach a dynamic equilibrium, the soil particles would migrate at a constant rate, which is defined as the electrophoretic mobility. Based on the measured electrophoretic mobility data, the Zeta potential of the soil particles can be quantitatively calculated by substituting the data into Henry's equation (Equation (1)). Henry's equation is as follows:

$$U_E = \frac{2\varepsilon\zeta \mathrm{f}(\kappa \mathrm{a})}{3\eta} \quad (1)$$

where U_E is the electrophoretic mobility, ε is the dielectric constant, ζ is the Zeta potential, η is the viscosity, $\mathrm{f}(\kappa \mathrm{a})$ is the Henry's constant.

2.2.3. Dynamic Light Scattering (DLS) Tests

DLS tests are a commonly used experimental method for studying changes in particle size. The dynamic light scattering test was conducted on the high-clay-content soil sample ($Q_8F_2M_{15}K_{15}$) prepared earlier. The preparation of the colloidal suspension was carried out using a combination of ultrasonic dispersion and static sedimentation siphon methods [25]. The specific procedure is as follows: (a) 50 g of marine clay soil sample was weighed and placed into a 500 mL beaker, then an appropriate amount of deionized water was added for initial dispersion. After that, more deionized water was added to bring the volume up to the 500 mL mark, and the pH of the system was adjusted to 7.4–7.6 using a 0.1 mol/L sodium hydroxide solution. (b) The dispersion was placed on a magnetic stirrer, and the soil sample was continuously stirred at a speed of 200–300 r/min for 15 min to ensure thorough mixing of the soil and water. (c) The stirred suspension was transferred to an ultrasonic oscillator, where it was subjected to ultrasonic dispersion at 25 °C for 15 min to break up soil aggregates and achieve uniform dispersion. (d) After ultrasonic treatment, the suspension was transferred to a 5 L beaker and diluted with deionized water up to the 5 L mark. After thoroughly mixing with a magnetic stirrer, the solution was placed in a dark environment at 25 °C to stand. The theoretical sedimentation time for particles smaller than 700 nm, calculated using Stokes' law, was determined by observing the sedimentation

of the particles over 10 cm. (e) After standing for the theoretical settling time, a siphon tube (made of PU material, with an inner diameter of 10 mm, outer diameter of 12 mm, and a length of 1 m) was used to slowly extract the upper suspension from 2 cm below the liquid surface. The extraction process was repeated until no noticeable particle settling occurred after the upper suspension had stood for 5 min. The particle size of the marine clay colloidal particles, as measured by the DLS instrument, was found to be 597 nm for the initial effective hydrodynamic diameter.

The DLS test in this experiment was performed using the BI-200SM wide-angle dynamic/static light scattering instrument produced by Brookhaven Instruments (New York, NY, USA). The temperature of the test chamber was precisely controlled at 298.15 K. The specific procedure for DLS testing is as follows: (a) A stock solution of marine clay colloid with a mass concentration of 2 g/L was prepared using deionized water as the dispersion medium. The stock solution was then transferred to an ultrasonic crusher (SB-4200DT, Xinzhi Biotechnology Co., Ltd., Hangzhou, China) for 10 min of ultrasonic treatment to ensure uniform dispersion of the colloidal particles. (b) Based on the colloidal stock solution, a series of experimental samples were prepared with ionic strength gradients set at 0%, 1%, 2.5%, 5%, and 10%. Each sample was diluted with deionized water to a final volume of 10 mL to ensure consistent sample volume for testing. (c) The prepared experimental samples were thoroughly mixed by shaking, and then the particle aggregation process monitoring program was initiated. The laser scattering instrument's built-in data acquisition system was used to automatically record the particle size and size distribution characteristics of the aggregates. The temperature was maintained at 25 $\pm$ 0.5 °C throughout the test, which were continuously monitored for 30 min, recording one set of valid data every 30 s.

3. Results and Discussions

3.1. Analysis of ESEM Test Results

3.1.1. ESEM Images of Four Original Minerals

ESEM observations were conducted on the four minerals to clarify their microstructural characteristics, providing fundamental support for subsequent observation, analysis, and comparative studies of the soil samples. As shown in Figure 1, at 2000$\times$ magnification, the particles of the four minerals each exhibit unique features. Quartz particles primarily appear angular, with clear crystal boundaries, and the surfaces are relatively smooth. The pores between the particles are quite noticeable (Figure 1a). Compared to quartz, feldspar particles exhibit a very clear layered structure. They appear as platy or blocky crystals, with parallel striations often visible across the crystal faces (Figure 1b). Montmorillonite particles tend to aggregate into flocculent masses, displaying a lamellar structure. The surface is smooth and exhibits distinct layering, a characteristic directly related to their significant water absorption and swelling properties when hydrated (Figure 1c). Kaolinite particles typically appear plate-like, and compared to montmorillonite, the connections between particles are relatively loose (Figure 1d).

3.1.2. Microstructural Responses to Salinity/Mineral Composition

The microstructural characteristics of soil specimens provide insight into the intrinsic mechanisms governing the evolution of their mechanical behavior [26]. Using ESEM, differences in mineralogical heterogeneity and structural variations induced by fluctuations in pore-water salinity can be directly identified from micrographs. Given that pore-water salinity is a key factor controlling the microstructure of the specimens, three salinity levels with pronounced gradients of 0%, 2.5%, and 10% were selected for comparative observation in this study. In addition, ESEM images acquired at different magnifications emphasize

different aspects of the microstructure. At a magnification of 2000, the overall morphology and spatial arrangement of particles can be clearly captured, thereby providing a basis for quantitative analyses of pore distribution patterns and pore morphological characteristics. In contrast, high-magnification images at 8000 enable refined characterization of interparticle contact modes and cementation states, and also allow effective identification of micropore distributions within particle aggregates.

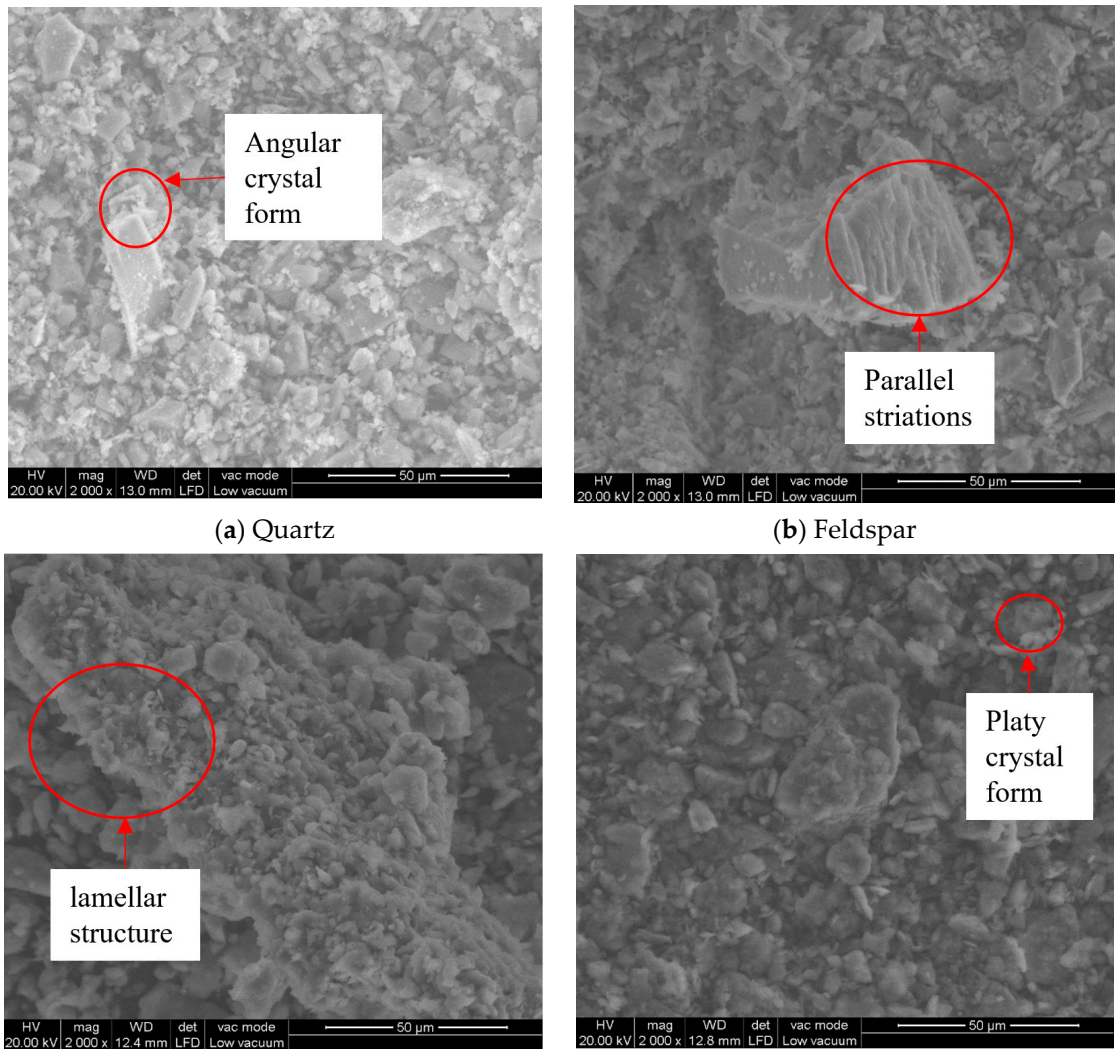


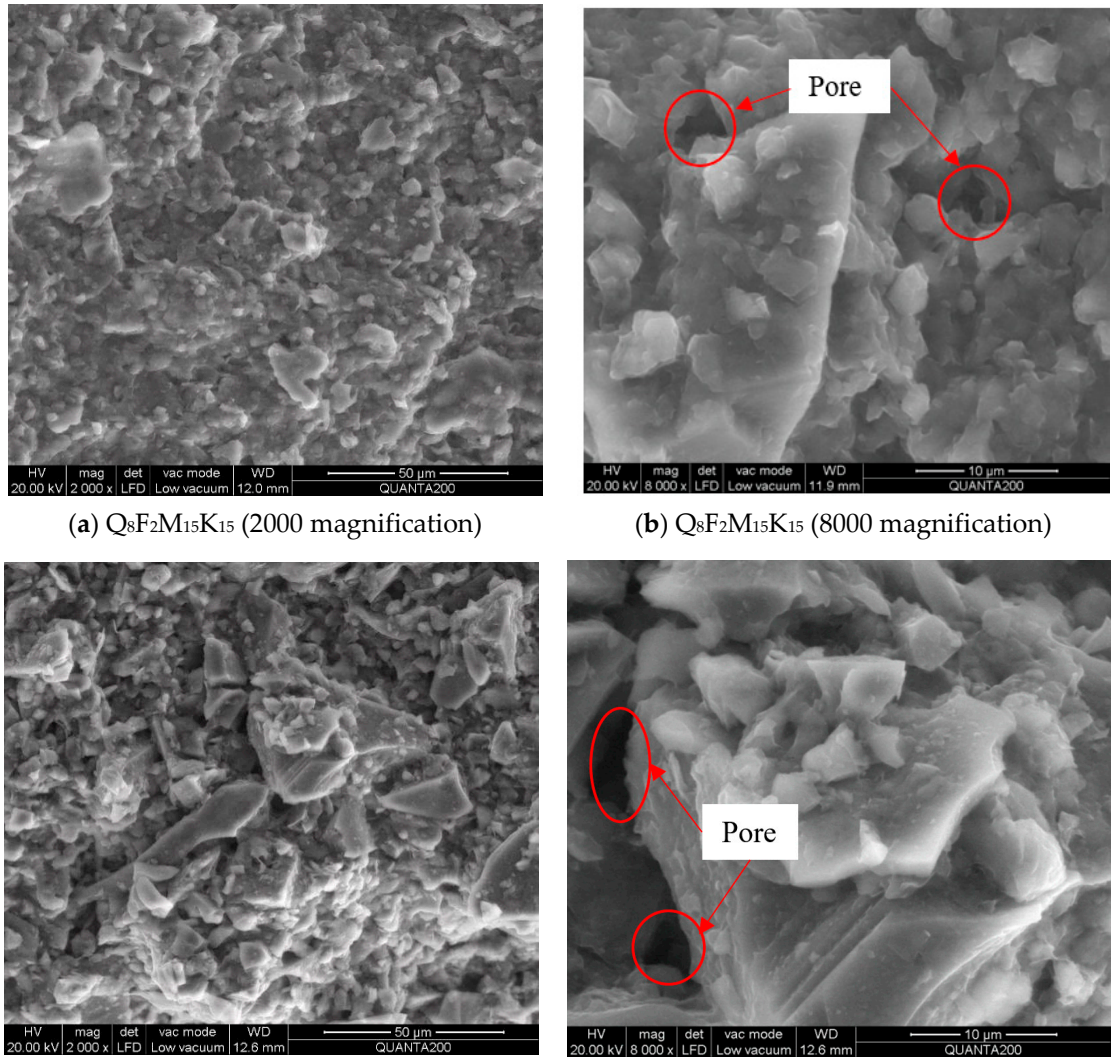
Figure 1. ESEM images of four original mineral particles (2000 magnification).

In microstructural analysis of soils, the investigation is typically conducted from three perspectives: particle morphology, particle arrangement and fabric, and interparticle contact relationships, in order to establish the intrinsic link between microstructural features and macroscopic mechanical responses [27]. As shown in Figure 2, the two artificially synthesized soil samples exhibit markedly different microstructural morphologies and fabric characteristics, driven by differences in mineral composition. First, from the perspective of particle morphology, the soil sample with a high clay mineral content, $Q_8F_2M_{15}K_{15}$ (Figure 2a), exhibits a typical clod-like aggregated appearance. In contrast, the soil sample with a lower clay mineral content, $Q_{24}F_6M_5K_5$, displays a morphology closer to a granular structure, in which the non-clay mineral framework is more pronounced, particle edges and outlines are clearer, and fine particles mainly occur as point-like or thin-layer attachments on the surfaces of framework grains, resulting in an overall looser structure. Second, in

terms of particle arrangement and fabric, $Q_8F_2M_{15}K_{15}$ tends to form a flocculated structure under non-saline conditions. Under the competition between electrostatic repulsion and van der Waals attraction, clay platelets commonly connect through edge–face and face–face contacts, forming a three-dimensional flocculated framework and giving rise to locally "open–bridged" aggregate structures. By contrast, $Q_{24}F_6M_5K_5$ more closely resembles a honeycomb-like fabric, in which a relatively continuous pore network develops between coarse framework particles, exhibiting more pronounced pore connectivity and openness. Third, analysis of interparticle contact relationships and connection modes indicates that $Q_8F_2M_{15}K_{15}$ exhibits a higher degree of complexity and compactness in particle connections. Compared with the relatively simple edge–edge, edge–face, and face–face contacts shown in Figure 2c, clay particles in $Q_8F_2M_{15}K_{15}$ more readily form "cemented–bridged" connections between non-clay mineral grains, constructing continuous interparticle contact chains and local aggregates within the framework. This significantly enhances the continuity and stability of the contact network. Such a denser flocculated framework also implies that the structural strength and deformation resistance of $Q_8F_2M_{15}K_{15}$ are more readily supported at the microscale. Finally, high-magnification images further reveal that, owing to the higher clay content in $Q_8F_2M_{15}K_{15}$, a substantially larger number of clay particles adhere to and envelop the surfaces and surrounding regions of non-clay minerals such as quartz and feldspar. The filling and blocking effects of fine particles on pores are therefore more pronounced, leading to smaller interparticle micropore sizes and a more localized pore distribution. In contrast, in $Q_{24}F_6M_5K_5$, the degree of clay particle coating and pore filling is relatively weak, resulting in more open pores with larger characteristic sizes.

A comparative analysis of Figures 2–4 clearly demonstrates that the regulatory effect of pore-water salinity on soil structure is distinctly manifested at the microscale. Taking the high-clay-content soil sample $Q_8F_2M_{15}K_{15}$ as an example, comparison of its ESEM images under different pore-water salinity conditions (Figures 2a, 3a and 4a) shows that, with the gradual increase in salinity, salt-induced flocculation structures progressively appear on mineral particle surfaces and within interparticle connection zones. Accordingly, the overall microstructural fabric evolves from a relatively dispersed state toward a more flocculated configuration, and the microstructure of $Q_8F_2M_{15}K_{15}$ exhibits a consistent evolutionary trend. Further analysis of high-magnification images (Figures 2b,d and 3b,d) indicates that at a salinity of 2.5% a certain degree of salt-induced flocculation is observed between particles; these newly formed flocculent features do not yet function as stable bridges. Instead, they may locally disturb the original connections formed between clay platelets and non-clay mineral framework particles, weakening or separating some pre-existing contacts. As a result, the number of interparticle micropores increases and the pore structure becomes looser. This stage of transient structural loosening reflects an intermediate salinity condition, under which flocculation has not yet developed into a stable framework. When the pore-water salinity is further increased to 10% (Figure 4b,d), both the abundance and continuity of salt flocs are significantly enhanced. These salt-induced flocculation structures progressively exert a more pronounced bridging and filling effect between particles, allowing previously separated particles to re-establish contacts and leading to a more continuous and compact interparticle contact network. Correspondingly, both the number and size of interparticle micropores are markedly reduced, and the overall structure becomes denser and more stable, indicating that the system has transitioned from a "transitional flocculation" stage to a relatively mature flocculated framework. During the increase in pore-water salinity from 0 to 2.5%, the microstructure is characterized by temporary loosening and an increase in pore volume, whereas a further increase in salinity to 10% promotes the stable establishment of a flocculated framework and structural densification. Overall, these observations indicate that pore-water salinity governs the

staged reconstruction of soil microstructure by regulating the processes of flocculation, separation, and re-bridging between particles.

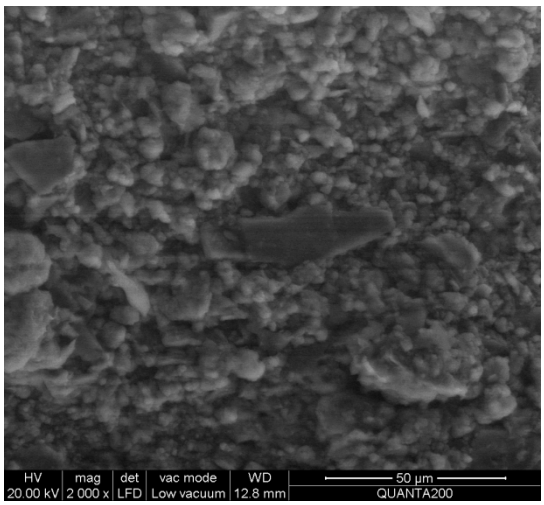


(**a**) $Q_8F_2M_{15}K_{15}$ (2000 magnification) (**b**) $Q_8F_2M_{15}K_{15}$ (8000 magnification)

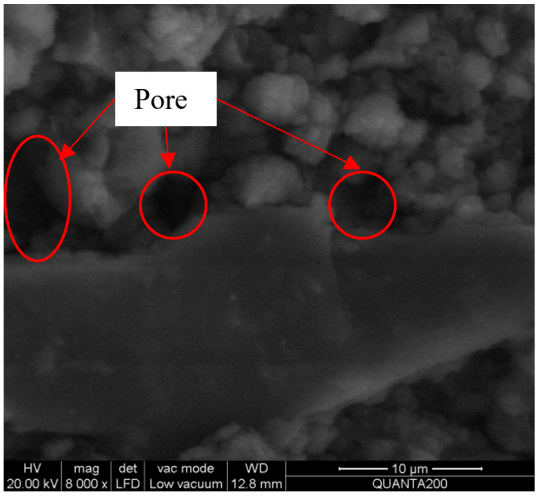
(**c**) $Q_{24}F_6M_5K_5$ (2000 magnification) (**d**) $Q_{24}F_6M_5K_5$ (8000 magnification)

Figure 2. ESEM images of soil samples $Q_8F_2M_{15}K_{15}$ and $Q_{24}F_6M_5K_5$ with 0% salinity.

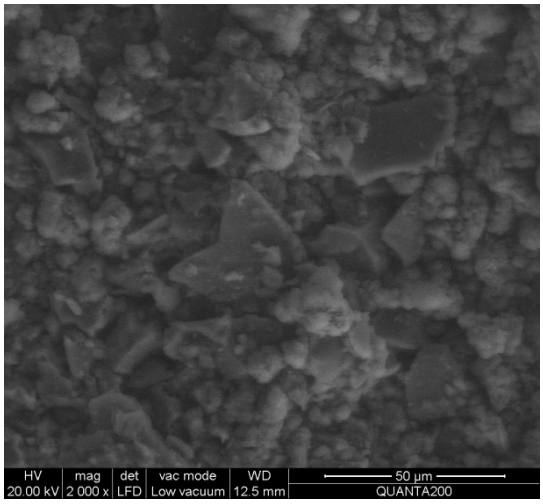
After analyzing the microstructure of the soil samples, in order to gain deeper insight into the microscopic factors influencing soil structure, the ESEM images were further processed using the image analysis software ImageJ (ImageJ bundled with 64-bit Java 8), and relevant microstructural parameters were extracted. First, the original ESEM images were adjusted in terms of brightness and contrast using Photoshop 2024 to enhance image clarity. Subsequently, the images were converted into grayscale images in ImageJ, and appropriate threshold values were determined. The grayscale images were then transformed into binary images based on the selected thresholds, in which pores and soil particles were distinguished by black and white pixels, respectively. During this process, the threshold values were iteratively adjusted and refined, ultimately yielding the images shown in Figures 5–7. By processing the binarized images, ImageJ was further employed to extract the pore area ratio, which quantitatively reflects the distribution characteristics of interparticle voids to a certain extent.



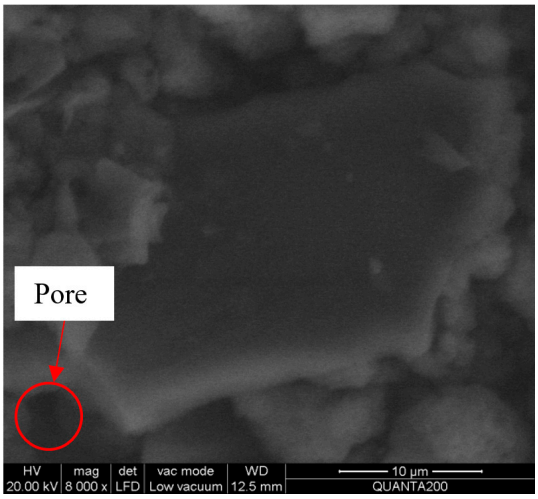
(**a**) $Q_8F_2M_{15}K_{15}$ (2000 magnification)



(**b**) $Q_8F_2M_{15}K_{15}$ (8000 magnification)

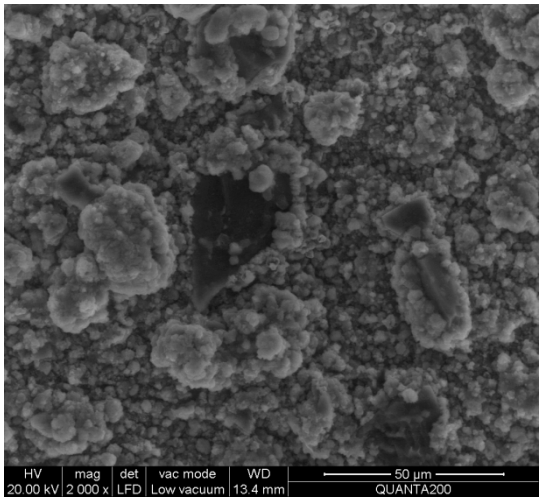


(**c**) $Q_{24}F_6M_5K_5$ (2000 magnification)

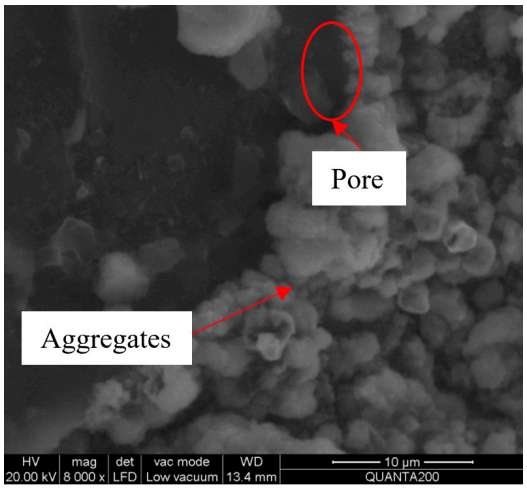


(**d**) $Q_{24}F_6M_5K_5$ (8000 magnification)

Figure 3. ESEM images of soil samples $Q_8F_2M_{15}K_{15}$ and $Q_{24}F_6M_5K_5$ with 2.5% salinity.

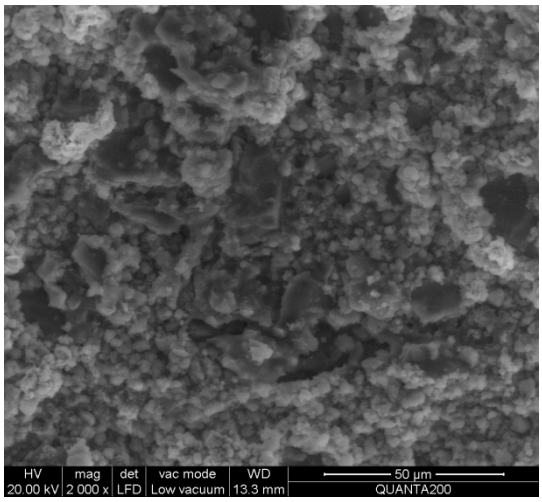


(**a**) $Q_8F_2M_{15}K_{15}$ (2000 magnification)

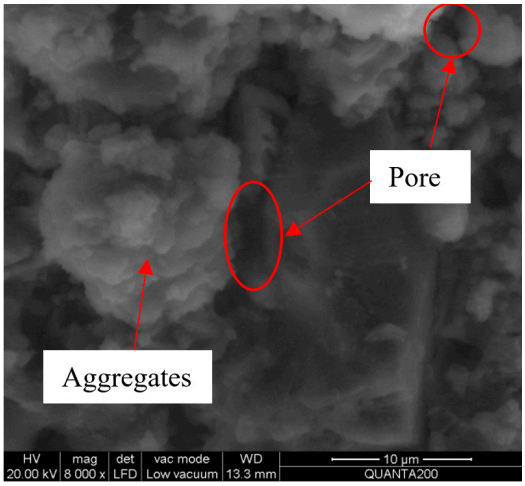


(**b**) $Q_8F_2M_{15}K_{15}$ (8000 magnification)

Figure 4. *Cont.*

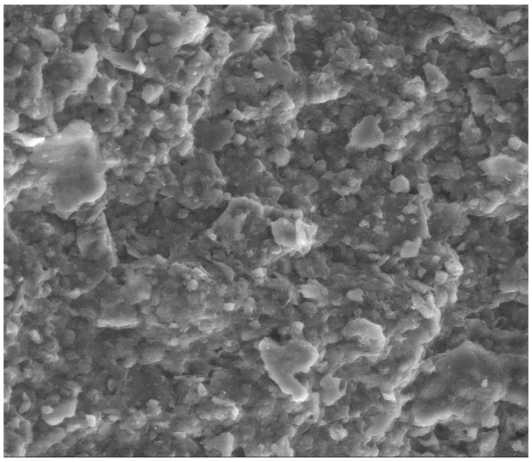


(**c**) $Q_{24}F_6M_5K_5$ (2000 magnification)

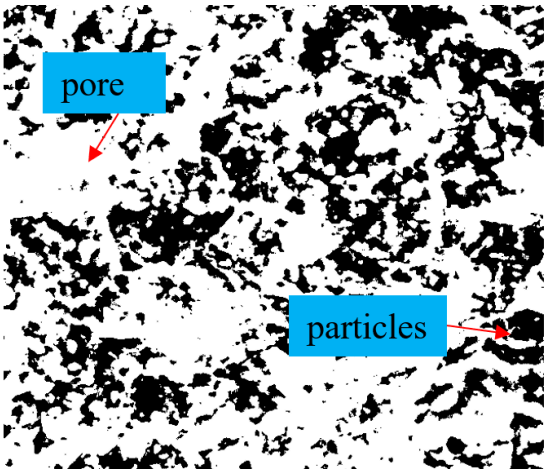


(**d**) $Q_{24}F_6M_5K_5$ (8000 magnification)

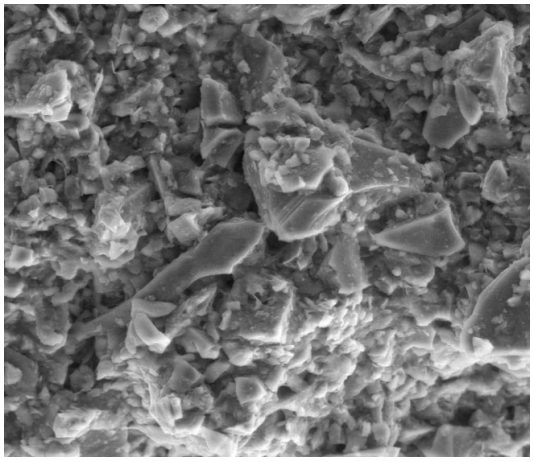
Figure 4. ESEM images of soil samples $Q_8F_2M_{15}K_{15}$ and $Q_{24}F_6M_5K_5$ with 10% salinity.



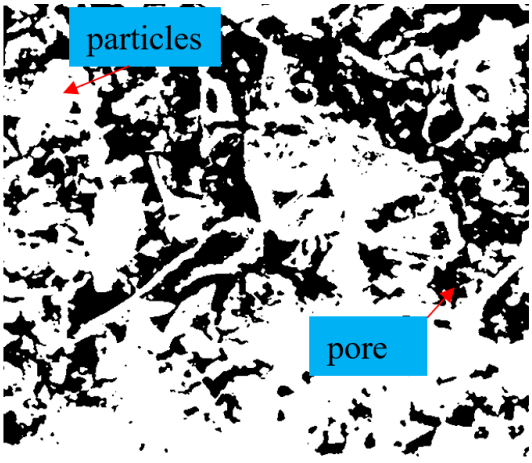
(**a**) $Q_8F_2M_{15}K_{15}$ (2000 magnification) grayscale image



(**b**) $Q_8F_2M_{15}K_{15}$ (2000 magnification) binarized image

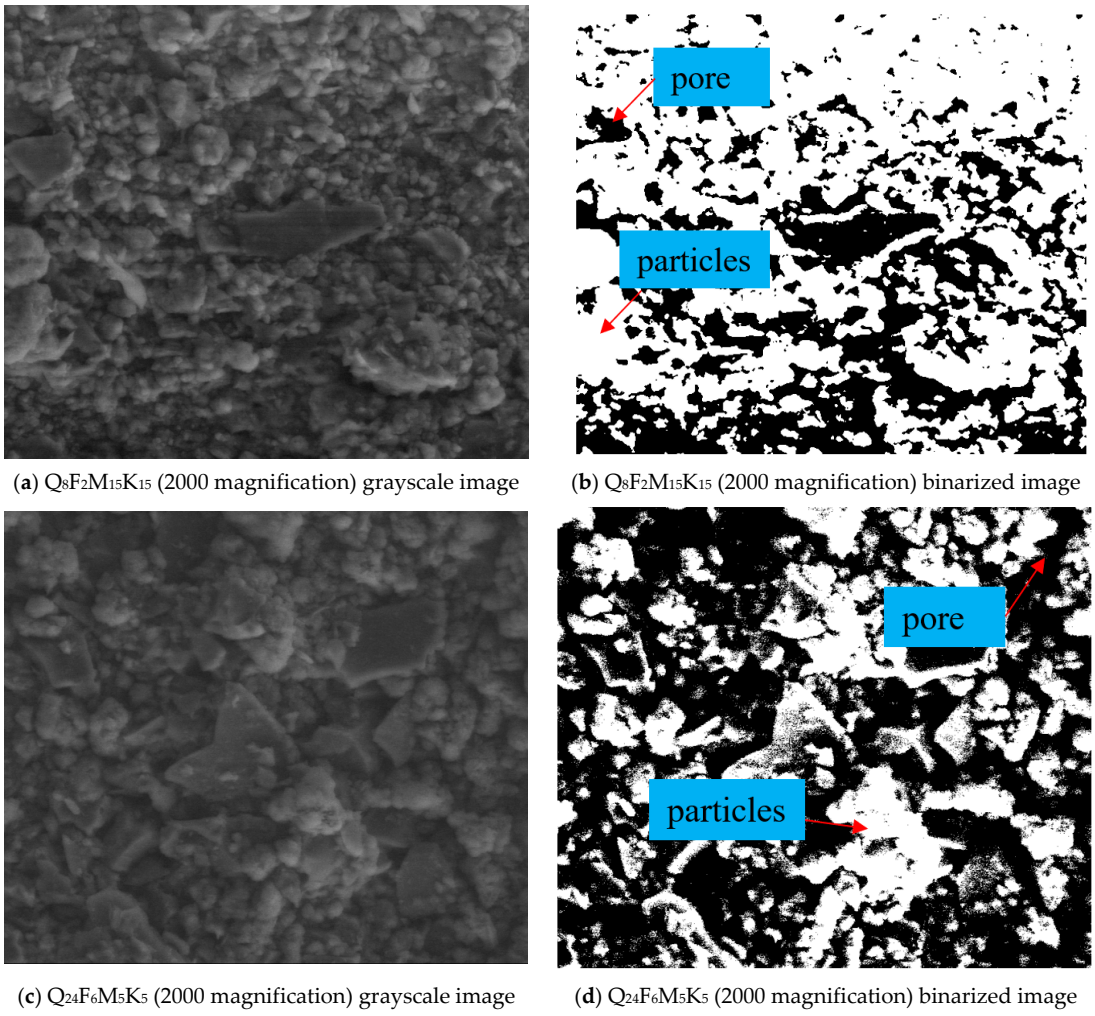


(**c**) $Q_{24}F_6M_5K_5$ (2000 magnification) grayscale image



(**d**) $Q_{24}F_6M_5K_5$ (2000 magnification) binarized image

Figure 5. ESEM grayscale images and binarized images of soil samples $Q_8F_2M_{15}K_{15}$ and $Q_{24}F_6M_5K_5$ with 0% salinity.



(**a**) $Q_8F_2M_{15}K_{15}$ (2000 magnification) grayscale image (**b**) $Q_8F_2M_{15}K_{15}$ (2000 magnification) binarized image

(**c**) $Q_{24}F_6M_5K_5$ (2000 magnification) grayscale image (**d**) $Q_{24}F_6M_5K_5$ (2000 magnification) binarized image

Figure 6. ESEM grayscale images and binarized images of soil samples $Q_8F_2M_{15}K_{15}$ and $Q_{24}F_6M_5K_5$ with 2.5% salinity.

Porosity is defined as the ratio of the pore area to the total area in the binarized ESEM images, where white represents particles and black represents pores. However, there is a certain discrepancy between this value and the actual porosity of the soil mass. Due to the unevenness of the mineral surface, some particles may be misidentified as pores, which results in an overestimated porosity. Nevertheless, the porosity of the microstructure can still reflect the physical properties of the soil mass to a certain extent. ESEM images of the two soil samples under three pore-water salinity conditions were processed to analyze their pore characteristics.

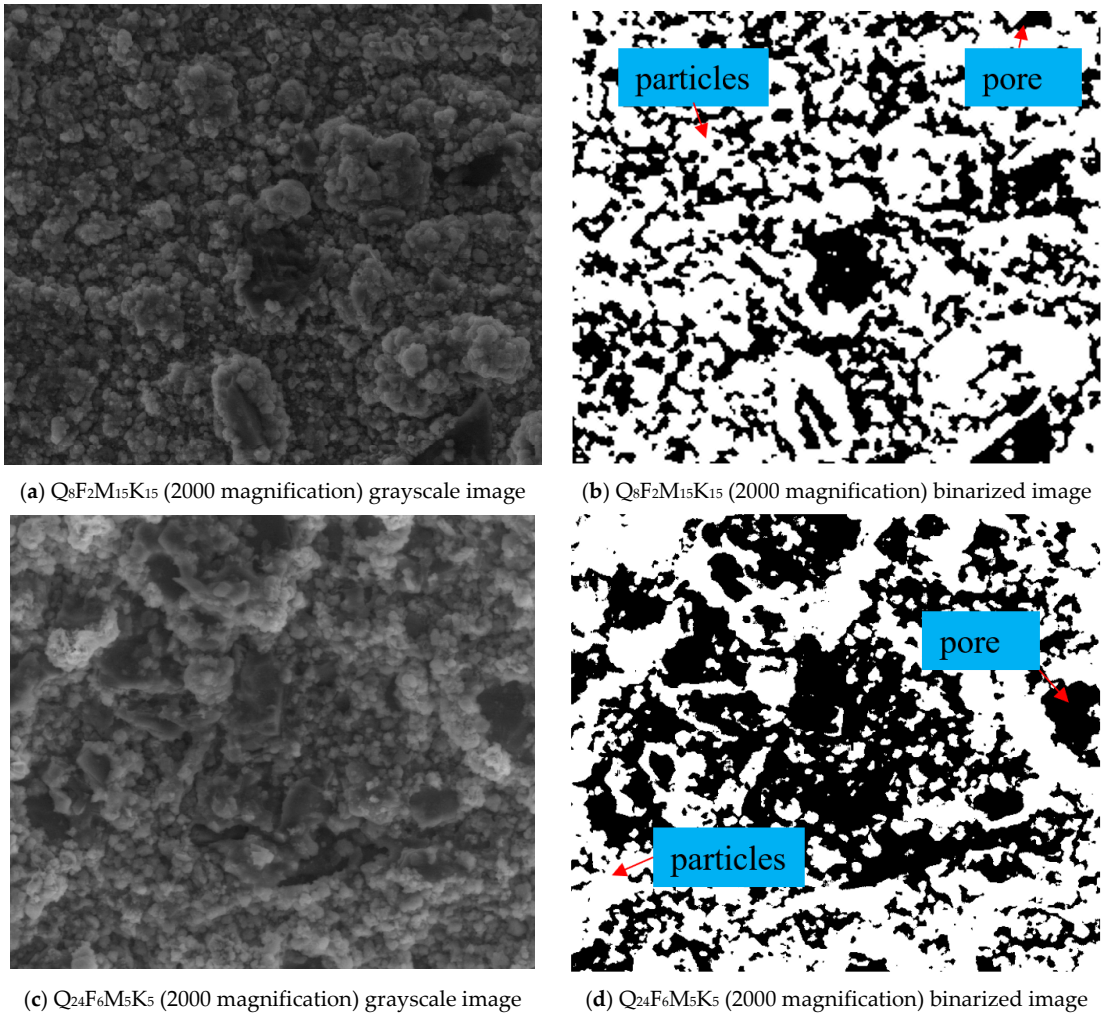
The porosity is calculated as follows:

$$n_{ESEM} = \frac{S_V}{S} \times 100\% \quad (2)$$

where n_{ESEM} denotes the porosity obtained from the binarized image, S_V represents the area occupied by pores, and S is the total area of the image.

According to the calculated results presented in Table 2, a comparison between soil sample $Q_8F_2M_{15}K_{15}$ and soil sample $Q_{24}F_6M_5K_5$ under the 0% condition indicates that, in the absence of salt-induced flocculation associated with pore-water salinity, the soil sample with a higher clay mass fraction exhibits a lower porosity. This result suggests that particles in the high-clay-content soil sample are more tightly connected, with fewer voids between particles of different mineral compositions. As pore-water salinity varies, salt-induced

flocculation begins to occur between particles, leading to an increase in porosity to some extent. This phenomenon is more pronounced in the soil sample with a higher clay mass fraction. One possible reason is that pore-water salinity affects the bound water layers associated with clay particles, thereby weakening interparticle bonding and promoting the development of interparticle voids.



(**a**) $Q_8F_2M_{15}K_{15}$ (2000 magnification) grayscale image (**b**) $Q_8F_2M_{15}K_{15}$ (2000 magnification) binarized image

(**c**) $Q_{24}F_6M_5K_5$ (2000 magnification) grayscale image (**d**) $Q_{24}F_6M_5K_5$ (2000 magnification) binarized image

Figure 7. ESEM grayscale images and binarized images of soil samples $Q_8F_2M_{15}K_{15}$ and $Q_{24}F_6M_5K_5$ with 10% salinity.

Table 2. Porosity calculation of marine clay based on ESEM tests.

Soil Sample	Porosity (%)		
	0%	2.5%	10%
$Q_8F_2M_{15}K_{15}$	32.15	34.10	36.66
$Q_{24}F_6M_5K_5$	34.83	37.40	46.82

3.2. Analysis of Surface Potential Results and Influencing Factors of Soil

In the field of microstructural research on soils, in addition to focusing on the characterization and analysis of the soil microstructure, the electrical potential characteristics of soil particle surfaces and their variations are also important microscopic factors for representing the mechanical properties of clay. Although the surface potential of soil samples cannot be directly tested, the Zeta potential, which is closely related to surface potential, can be obtained through experimental testing [28]. As shown in Figure 8, when clay particles inter-

act with water, the surface of the soil particles carries a negative charge, which affects the distribution of ions in the solution at the particle-solution interface. Due to the electrostatic attraction between positive and negative charges, cations gather around the surface of the clay particles, forming a double layer structure. The double layer consists of two main regions: the inner region, also known as the Stern layer, where ions are tightly bound to the surface of the particles, and the diffuse region, where there is a sliding interface. At this interface, the ions form a stable relationship with the particles and move with the movement of the particles. However, ions outside the sliding interface do not move with the particles, a phenomenon known as the electrokinetic effect. There is a potential difference at the sliding surface between the clay particles and the surrounding aqueous solution, and the potential difference between this interface and the bulk solution far from the particles is called the Zeta potential (ζ). Zeta potential is the core parameter that characterizes the double layer properties of the clay-water system.

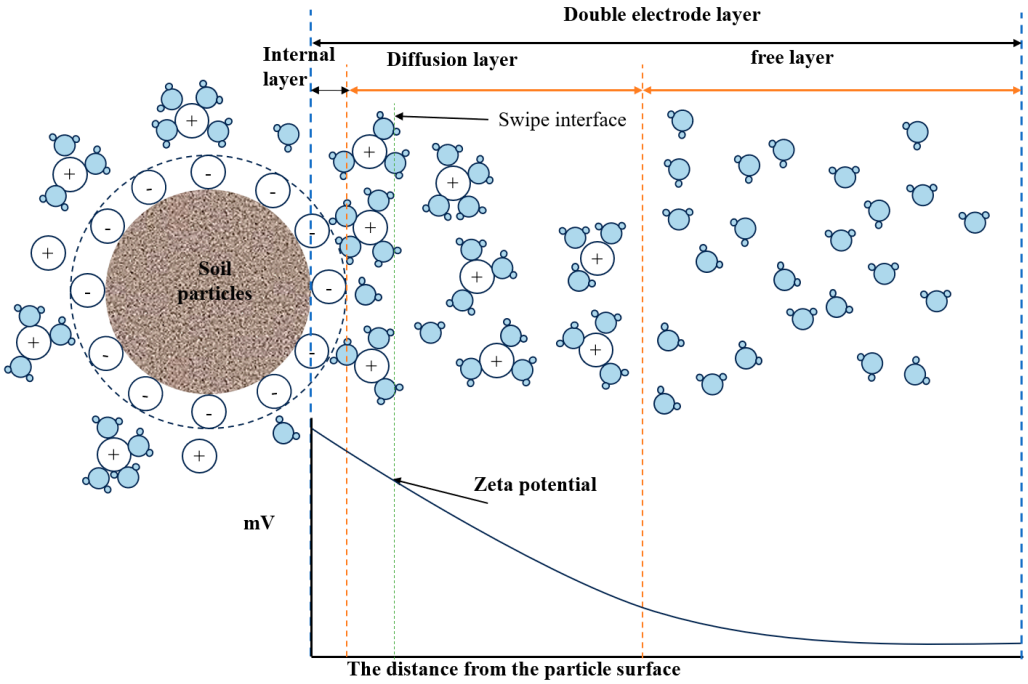


Figure 8. Schema of Zeta potential difference as a function of distance from the charged surface of particles in suspension (Revised from [28]).

By measuring the Zeta potential of soil samples, it can be found that the higher the Zeta potential, the greater the electrostatic repulsion between soil particles. The introduction of NaCl solution leads to the compression of the electrical double layer thickness with the increase in ion concentration in the solution; this disrupts and readjusts the interparticle force balance, causing the overlapping of the electrical double layer and thus a reduction in the interparticle spatial volume. In contrast, the Van der Waals attractive force remains unchanged, which ultimately results in an increased degree of particle aggregation. Therefore, selecting the Zeta potential as an index to characterize the magnitude of electrostatic repulsion allows for an effective judgment of the flocculation or dispersion degree of clay particles in soil.

The obtained Zeta potential distribution curves are shown in Figure 9a, where the peak of each curve corresponds to the Zeta potential value of the tested soil sample. The relationships between Zeta potential and salinity for soil samples $Q_8F_2M_{15}K_{15}$ and $Q_{24}F_6M_5K_5$ under different salinity conditions are presented in Figure 9b. As shown in Figure 9b, with increasing salinity, the Zeta potential of soil sample $Q_{24}F_6M_5K_5$ gradually

decreases from approximately −37 to −34 mV to about −10 to 0 mV. Similarly, as salinity increases from 0% to 10%, the Zeta potential of soil sample $Q_8F_2M_{15}K_{15}$ decreases from about −25 to −20 mV to −8 to −6 mV. At a salinity of 1%, the Zeta potential of soil sample $Q_8F_2M_{15}K_{15}$ exhibits an upward trend, peaking at −28 to −22 mV, and subsequently undergoes a gradual decline with further increases in salinity.

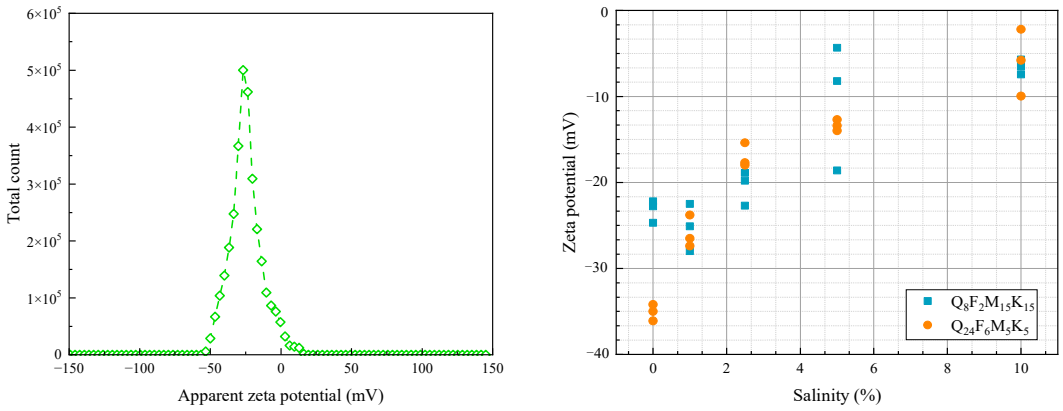


Figure 9. Zeta potential of soil samples. (**a**) Zeta potential distribution curves. (**b**) Zeta potential of soil samples under different salinities.

Riddick [29] investigated variations in Zeta potential and proposed the relationship between Zeta potential and colloidal flocculation or dispersion behavior, as summarized in Table 3. Combined with the results shown in Figure 9, it can be observed that with increasing salinity, the particle behavior of soil sample $Q_{24}F_6M_5K_5$ gradually shifts from a stable state toward the onset of aggregation. For soil sample $Q_8F_2M_{15}K_{15}$, its degree of dispersion initially increases with salinity; however, as salinity increases from 1% to 10%, the particles begin to undergo rapid aggregation. Furthermore, Li et al. [30] conducted Zeta potential tests on four individual mineral components and found that, with increasing mass fraction, the Zeta potential of montmorillonite minerals gradually decreases, approaching −60 mV. This implies that, from a macroscopic mechanical perspective, a higher salinity may be required to induce such transitional behavior as the mass fraction of clay particles increases.

Table 3. Relationship between Zeta potential and colloidal stability (Riddick, 1968) [29].

Zeta Potential (mV)	**0 to ±5**	**±10 to ±30**	**±30 to ±40**	**±40 to ±50**	**±50 to ±60**
Colloidal stability	Rapid aggregation	Onset of aggregation	Moderate stability	Good stability	Excellent stability

A further analysis of the microstructural characteristics of the soil samples is conducted. Differences in soil pore structures arise, on the one hand, from variations in the arrangement and connection modes of different minerals within the soil matrix. Such differences in porosity can lead to changes in the mechanical properties of the soil; soils with a greater number of larger pores are more prone to deformation and energy dissipation when subjected to external loading. On the other hand, differences in particle surface potential induced by variations in mineral composition and salinity conditions also constitute an important factor governing structural heterogeneity. Compared with non-clay minerals, clay minerals exhibit a stronger ability to form stable structures through the interaction between surface charges and adsorbed cations, as evidenced by the Zeta potential test results. Moreover, differences in ionic concentration and adsorption capacity in the pore

solution further influence the aggregation behavior of mineral particles, promoting the formation of more stable particle assemblages.

3.3. Particle Size Analysis Under Salinity Disturbance

DLS tests are based on the principles of light scattering and Brownian motion. By analyzing the temporal fluctuations of scattered light intensity, the effective hydrodynamic diameter of particles can be obtained. Consequently, DLS not only enables the characterization of particle size and size distribution in suspension systems, but also allows real-time tracking of the evolution of particles from a dispersed state to an aggregated state. This approach further reveals the response of particle aggregates to variations in ionic concentration in the solution and provides a quantitative characterization of aggregation kinetics.

In this study, a soil sample with a high clay mineral content ($Q_8F_2M_{15}K_{15}$) was selected for DLS testing to enhance sensitivity to salinity-induced disturbances. As shown in Figure 10 with increasing observation time, the effective hydrodynamic diameter of clay mineral particles under different salinity conditions exhibits an overall increasing trend, indicating that pronounced aggregation occurs in the suspension. Overall, the particle-size evolution curves display a distinct two-stage behavior. In the initial stage, rapid growth is observed, corresponding to a high frequency of interparticle collisions and the rapid formation and expansion of aggregates. In the later stage, the growth rate gradually decreases and approaches a stable plateau, suggesting that the system progressively reaches a dynamic equilibrium, where particle aggregation is jointly constrained by spatial hindrance, densification of aggregate structures, and limitations imposed by shear and diffusion processes, resulting in a stabilized aggregate size.

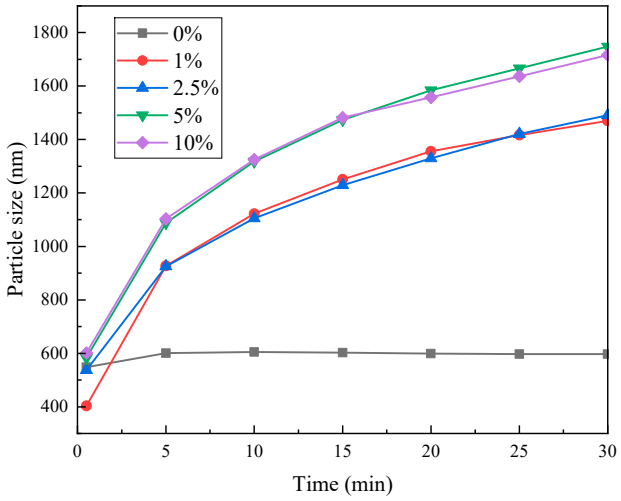


Figure 10. Particle sizes of soil samples at different salinities after 30 min.

Further comparison among different salinity conditions reveals that salinity perturbations significantly amplify the aggregation behavior of clay particles. In pure water, the overall aggregate size of clay particles remains relatively small, with noticeable growth mainly occurring within the first approximately 5 min, after which the curves rapidly reach a steady state. This behavior indicates that under low ionic strength conditions, strong electrostatic repulsion between particles limits aggregation, and the system tends to maintain a relatively stable dispersed state. In contrast, in saline solutions, the aggregation process of clay particles is markedly accelerated, with particle size increasing more rapidly and over a longer duration. This trend reflects the compression of the electrical double layer and the consequent reduction in electrostatic repulsion due to increased ionic strength, which significantly enhances the probability of effective interparticle collisions and adhesion. Par-

ticularly under high-salinity conditions, the particle-size growth rate is further increased, and aggregates evolve more rapidly toward larger characteristic scales, indicating that salinity exerts a stronger promoting effect on clay particle coagulation and may correspond to more pronounced formation of flocculated frameworks and microstructural reorganization.

Figure 10 illustrates the response of the characteristic aggregate size to salinity once the system had reached a relatively stable stage. As salinity increases from 0% to 10%, the aggregate size exhibits a non-monotonic trend, characterized by an initial rapid increase followed by a slight decrease, indicating that salinity exerts a complex, multi-mechanistic influence on the particle aggregation process. Under pure water conditions (0% salinity), the ionic strength of the pore fluid is low, resulting in a relatively thick electrical double layer on the surfaces of clay particles. Interparticle interactions are therefore dominated by electrostatic repulsion, creating a high energy barrier that inhibits aggregation following effective collisions. Consequently, the system tends to maintain a relatively stable dispersed state, and the aggregate size at 30 min remains small. With increasing salinity, the introduction of Na^+ ions significantly enhance the ionic strength of the solution, leading to compression of the electrical double layer and a reduction in the Debye length, thereby weakening electrostatic repulsion between particles. At the same time, Na^+ ions can adsorb onto or screen negatively charged sites on the surfaces of clay minerals, further reducing the effective interparticle energy barrier. In this stage, van der Waals attraction and other short-range interactions are more likely to dominate, facilitating particle adhesion and rapid aggregation. As a result, the aggregate size increases markedly with increasing salinity. However, when salinity is further increased to a high level (10%), the aggregation mechanism may shift from gradual cluster growth to rapid flocculation accompanied by structural reorganization. On the one hand, stronger electrostatic screening under high ionic strength conditions promotes the formation of flocs. On the other hand, during floc formation, aggregates may undergo denser rearrangement or compaction of loosely bound clusters, such that the hydrodynamic size of the aggregates no longer increases monotonically but instead shows a slight decrease at the stable stage. Therefore, the reduction in aggregate size observed at 10% salinity can be interpreted as the combined effect of salinity-induced floc structural adjustment and densification.

4. Conclusions

In this study, the microstructure of soil samples was systematically investigated using ESEM, and the microstructural characteristics were quantitatively analyzed through porosity parameters. In addition, Zeta potential tests were conducted to examine the electrical double-layer structure of soil particles under different salinity conditions. Finally, DLS tests were employed to quantify the influence of salinity on the particle aggregation process. The microstructural investigations mainly focused on the high–clay-content soil sample $Q_8F_2M_{15}K_{15}$ and the low–clay-content soil sample $Q_{24}F_6M_5K_5$ under varying salinity conditions, and the main conclusions are summarized as follows:

1. Soil samples with different mineral compositions exhibited distinct characteristics in terms of particle morphology, particle arrangement, and interparticle contact relationships at the microstructural scale. Variations in mineral composition significantly modified the soil fabric and pore structure. Soils with a high clay mineral content typically displayed clod-like morphologies and well-developed flocculated skeleton structures, characterized by stronger particle coating, bridging, and cementation effects. As a result, the interparticle contact network became more continuous and compact, and the scale of micropores was reduced.
2. Fundamental differences in surface charge properties and cation adsorption capacities among mineral components lead to variations in the stability of the electrical double

layer and the mechanisms governing interparticle interactions. These differences, in turn, give rise to distinct pore structures and macroscopic mechanical responses. Compared with non-clay minerals, clay minerals are more prone to forming stable structures through surface charge–cation adsorption mechanisms, resulting in a more pronounced sensitivity to flocculation.

3. At low salinity, the microstructure is dominated by a particle-skeleton framework, with relatively high Zeta potential and small floc/agglomerate size. As salinity increases, the thickness of the electrical double layer changes, leading to pronounced microstructural evolution: the Zeta potential decreases, and flocs exhibit stronger bridging and pore-filling effects. Consequently, the particle-contact network becomes more continuous and compact, the structural stability is enhanced, and the agglomerate size increases. Overall, the presence of salt alters the physical properties of soil particles to some extent.

This study used ESEM, Zeta potential, and DLS tests to investigate the microstructural characteristics of marine clay. However, there are still certain limitations. ESEM primarily focuses on the morphological features of the sample surface and could not provide sufficient detailed information about the deeper structure or internal microstructure. Zeta potential might not fully reflect the charge distribution and interparticle interactions in complex systems. DLS testing uses the hydrodynamic diameter for analysis, which may introduce objective errors. Future studies may employ more precise methods, such as AFM microscopy, which can allow real-time tracking and analysis of dynamic processes such as particle aggregation and changes in particle surface potential.

Author Contributions: S.Y.: Writing—original draft, Methodology, Conceptualization, Investigation, Formal analysis. Y.S.: Writing—original draft, Writing—review and editing, Methodology, Supervision, Conceptualization, Resources, Funding acquisition. Z.L.: Writing—original draft, Investigation, Methodology. H.X.: Methodology, Supervision, Resources. Y.L.: Supervision, Methodology, Funding acquisition, Conceptualization. J.C.: Methodology, Supervision, Resources, Conceptualization. All authors have read and agreed to the published version of the manuscript.

Funding: This research was funded by the National Natural Science Foundation of China (No. 52478392), Natural Science Foundation of Guangdong Province (No. 2025A1515011857), and Science and Technology Projects in Guangzhou (No. 2025A03J0046).

Data Availability Statement: The data that support the findings of this study are available from the corresponding author upon reasonable request.

Conflicts of Interest: He'an Xie was employed by HUASEN Engineering Technology Group Co., Ltd. The remaining authors declare that the research was conducted in the absence of any commercial or financial relationships that could be construed as a potential conflict of interest.

References

1. Qi, W.; Rui, S.; Guo, Z. Wave/Current–Structure–Seabed Interactions Around Offshore Foundations. *J. Mar. Sci. Eng.* **2025**, *13*, 1595. [CrossRef]
2. Wang, L.; Lei, H.; Bo, Y.; Jiang, M.; Wang, P.; Liu, M. Geotechnical Behavior of Soft Dredger Fill and Deep Sea Soft Clay. *IOP Conf. Ser. Earth Environ. Sci.* **2020**, *570*, 062036. [CrossRef]
3. Chen, B.; Zhang, W.; Luo, Z.; Zhang, X.; Xu, K.; Mao, W.; Wang, J.; Huang, Y.; Zheng, H. Experimental Investigation on the Dynamic Behavior and Undrained Strength of Undisturbed and Remolded Marine Clays. *Eng. Geol.* **2025**, *353*, 108110. [CrossRef]
4. Luo, F.; Zhang, G.; Yao, Y. Macro-Micro Tests of Cohesive Soil under Varied Normal and Shear Stresses Subjected to Drying-Wetting Cycles. *J. Rock Mech. Geotech. Eng.* **2025**, *17*, 5893–5905. [CrossRef]
5. Bourg, I.C.; Ajo-Franklin, J.B. Clay, Water, and Salt: Controls on the Permeability of Fine-Grained Sedimentary Rocks. *Acc. Chem. Res.* **2017**, *50*, 2067–2074. [CrossRef]
6. Carrier, B.; Wang, L.; Vandamme, M.; Pellenq, R.J.-M.; Bornert, M.; Tanguy, A.; Van Damme, H. ESEM Study of the Humidity-Induced Swelling of Clay Film. *Langmuir* **2013**, *29*, 12823–12833. [CrossRef] [PubMed]

7. Kimura, H.; Tanabe, H.; Shinoki, S. Zeta Potential as a Key Indicator of Network Structure and Rheological Behavior in Smectite Clay Dispersions. *Fluids* **2025**, *10*, 178. [CrossRef]
8. Javaheri, F.; Esfandiarpour-Boroujeni, I.; Farpoor, M.H.; Holthusen, D.; Stewart, R.D. Counterions, Smectite, and Palygorskite Increase Microstructural Stability of Saline-Sodic Soils. *Soil Tillage Res.* **2022**, *216*, 105258. [CrossRef]
9. McFarlane, A.; Bremmell, K.; Addai-Mensah, J. Microstructure, Rheology and Dewatering Behaviour of Smectite Dispersions during Orthokinetic Flocculation. *Miner. Eng.* **2005**, *18*, 1173–1182. [CrossRef]
10. Markgraf, W.; Moreno, F.; Horn, R. Quantification of Microstructural Changes in Salorthidic Fluvaquents Using Rheological and Particle Charge Techniques. *Vadose Zone J.* **2012**, *11*, vzj2011-0061. [CrossRef]
11. Baumgarten, W.; Neugebauer, T.; Fuchs, E.; Horn, R. Structural Stability of Marshland Soils of the Riparian Zone of the Tidal Elbe River. *Soil Tillage Res.* **2012**, *125*, 80–88. [CrossRef]
12. Ni, H.; Huang, Y. Rheological Study on Influence of Mineral Composition on Viscoelastic Properties of Clay. *Appl. Clay Sci.* **2020**, *187*, 105493. [CrossRef]
13. Luckham, P.F.; Rossi, S. The Colloidal and Rheological Properties of Bentonite Suspensions. *Adv. Colloid Interface Sci.* **1999**, *82*, 43–92. [CrossRef]
14. Shan, Y.; Wang, X.; Cui, J.; Mo, H.; Li, Y. Effects of Clay Mineral Composition on the Dynamic Properties and Fabric of Artificial Marine Clay. *J. Mar. Sci. Eng.* **2021**, *9*, 1216. [CrossRef]
15. Shan, Y.; Meng, Q.; Yu, S.; Mo, H.; Li, Y. Energy Based Cyclic Strength for the Influence of Mineral Composition on Artificial Marine Clay. *Eng. Geol.* **2020**, *274*, 105713. [CrossRef]
16. Li, L.; Wang, L.; Liu, Q. Effects of Salinity and pH on Clay Colloid Aggregation in Ion-Adsorption-Type Rare Earth Ore Suspensions by Light Scattering Analysis. *Minerals* **2022**, *13*, 38. [CrossRef]
17. Jia, Z.; Li, J.; Gao, L.; Yang, D.; Kanaev, A. Dynamic Light Scattering: A Powerful Tool for In Situ Nanoparticle Sizing. *Colloids Interfaces* **2023**, *7*, 15. [CrossRef]
18. Zhao, X.; Xu, S.; Zhou, H. A New Method for Measuring Fast Aggregation Rate Based on the Growth of the Colloidal Aggregate Size. *Colloid Interface Sci. Commun.* **2024**, *58*, 100764. [CrossRef]
19. Soler, J.M.; Steefel, C.I.; Gimmi, T.; Leupin, O.X.; Cloet, V. Modeling the Ionic Strength Effect on Diffusion in Clay. The DR-A Experiment at Mont Terri. *ACS Earth Space Chem.* **2019**, *3*, 442–451. [CrossRef]
20. Muniruzzaman, M.; Rolle, M. Impact of Diffuse Layer Processes on Contaminant Forward and Back Diffusion in Heterogeneous Sandy-Clayey Domains. *J. Contam. Hydrol.* **2021**, *237*, 103754. [CrossRef]
21. Shan, Y.; Lu, Z.; Cui, J.; Li, W.; Li, Y.; Sun, W. Rheological Study of the Effect of Clay Mineral Composition on Non-Linear Viscoelasticity. *Appl. Clay Sci.* **2024**, *249*, 107229. [CrossRef]
22. Lei, H.; Qi, Z.; Feng, S.; Lei, S. Macroscopic and Microscopic Investigation of the Structural Characteristics of Artificially Structured Marine Clay. *Soils Found.* **2022**, *62*, 101243. [CrossRef]
23. Geng, W.; Han, W.; Yin, J.; Lu, Z. Salinity Effects on the Strength and Morphological Indices of Soft Marine Clay. *Sci. Rep.* **2022**, *12*, 17563. [CrossRef]
24. Frangenberg, M.; Schmidt, A.M.; Wilkens, J. New Experimental Approach for the Proper Consideration of Stagnant and Diffuse Layer Conductivity in the Zeta Potential Determination. *Langmuir* **2025**, *41*, 5188–5201. [CrossRef]
25. Song, X.; Chen, Z.; Zhang, Q.; Zhang, Z.; Wen, Y. Control Mechanism of Short-Term Fertilization with Cattle Manure on the Release Characteristics of Soil Colloids in Farmland: Grain Size and Physicochemical Properties. *Environ. Sci. Eur.* **2024**, *36*, 136. [CrossRef]
26. Delage, P.; Tessier, D. Macroscopic Effects of Nano and Microscopic Phenomena in Clayey Soils and Clay Rocks. *Geomech. Energy Environ.* **2021**, *27*, 100177. [CrossRef]
27. Zhang, X.; Wang, G.; Liu, X.; Xu, Y.; Kong, L. Microstructural Analysis of Pore Characteristics of Natural Structured Clay. *Bull. Eng. Geol. Environ.* **2022**, *81*, 473. [CrossRef]
28. Kaya, A.; Ören, A.H.; Yükselen, Y. Settling of Kaolinite in Different Aqueous Environment. *Mar. Georesources Geotechnol.* **2006**, *24*, 203–218. [CrossRef]
29. Riddick, T.M. *Control of Colloid Stability Through Zeta Potential: With a Closing Chapter on Its Relationship to Cardiovascular Disease*; Zeta-Meter Incorporated: Harrisonburg, VA, USA, 1968.
30. Li, H.; Chen, J.; Peng, C.; Min, F.; Song, S. Salt Coagulation or Flocculation? In Situ Zeta Potential Study on Ion Correlation and Slime Coating with the Presence of Clay: A Case of Coal Slurry Aggregation. *Environ. Res.* **2020**, *189*, 109875. [CrossRef]

Disclaimer/Publisher's Note: The statements, opinions and data contained in all publications are solely those of the individual author(s) and contributor(s) and not of MDPI and/or the editor(s). MDPI and/or the editor(s) disclaim responsibility for any injury to people or property resulting from any ideas, methods, instructions or products referred to in the content.